Journal of Materials Chemistry A

ROYAL SOCIETY OF CHEMISTRY

PAPER

View Article Online
View Journal | View Issue

Cite this: J. Mater. Chem. A, 2025, 13, 39163

Catalytic oxidation of 5-hydroxymethylfurfural to 2,5-diformylfuran using MOF-808(Cu) under near ambient conditions

Fabio Raspante,[a] Xiang Zhou,[a] Donald R. Inns,[a] Nusik Gedikoglu,[a] Muralidharan Shanmugam,[b] Adam Brookfield,[b] Alexandros P. Katsoulidis[a] and Matthew J. Rosseinsky *[a]

Biomass conversion involves transforming sustainable feedstocks into valuable intermediates for the chemical industry. A key biomass-derived platform molecule, 5-hydroxymethylfurfural (HMF), can be converted into various intermediates, including 2,5-diformylfuran (DFF), which has several industrial applications due to its versatile chemical reactivity. Herein, Cu loaded MOF-808, with three different Cu loadings, were synthesised and tested as catalysts for the liquid phase selective oxidation of HMF to DFF with 2,2,6,6-tetramethylpiperidine-1-oxyl (TEMPO). X-ray diffraction (XRD) and X-ray absorption spectroscopy (XAS) were performed to assess the speciation of Cu, with the development of a structure model of MOF-808(Cu_3). The structural analysis reveals that single square planar Cu(II) sites are located near the Zr_6 cluster and are bonded by coordinating to oxygen atoms of capping MeOH and H_2O ligands. Amongst the synthesised catalysts, MOF-808(Cu_3) exhibited the highest catalytic activity after 12 h, achieving a high HMF conversion (95.5 ± 2.7%) and DFF yield (78.9 ± 1.3%) at 30 °C. The nature of the catalytic reaction is heterogeneous as the yield of DFF decreases after the removal of the solid catalyst. The demonstration of catalytic activity with high selectivity under near ambient conditions advances the application of porous metal–organic framework-based catalysts for selective liquid phase oxidations.

Received 19th June 2025
Accepted 12th October 2025

DOI: 10.1039/d5ta04979b

rsc.li/materials-a

1 Introduction

Interest in biomass waste as a renewable carbon source has increased in recent years, as biomass represents an efficient alternative to fossil resources, with a neutral carbon balance.[1] Converting biomass into different chemicals is not only essential for reducing reliance on fossil resources, but also for enhancing the impact of green chemistry and the corresponding environmental benefits.[2] A biomass platform chemical that has garnered considerable attention recently is 5-hydroxymethylfurfural (HMF), due to its reactive functional groups that can undergo a wide range of chemical reactions. HMF can be selectively hydrogenated to produce 2,5-bis(hydroxymethyl) furan (BHMF), tetrahydrofuran-2,5-diyldimethanol (THFDM) or undergo hydrogenolysis to yield 5-MF (5-methylfurfural).[3–6] The furan ring in HMF can also participate in other reactions, such as ring opening, to obtain levulinic acid, adipic acid, 1-hydroxyhexane-2,5-dione, and 2,5-hexanedione.[7,8] The oxidation of HMF yield molecules such as 2,5-diformylfuran (DFF), 5-hydroxymethyl-2-furancarboxylic acid (HMFCA), 5-formyl-2-furancarboxylic acid (FFCA), and 2,5-furandicarboxylic acid (FDCA) (Scheme 1). These examples underscore the versatility of HMF as a platform chemical for synthesising a wide range of molecules with various industrial applications.[3–5] Amongst these, DFF stands out due to its significant industrial potential, as it can be converted into valuable compounds like antifungal agents, furanic biopolymers and furan–urea resins.[9,10]

Several studies report the selective oxidation of HMF to DFF utilising both homogeneous and heterogeneous catalysts. Homogeneous catalysts such as CuCl and $Cu(NO_3)_2$ were tested in the HMF catalytic oxidation at room temperature and 50 °C, respectively, with more than 80% of HMF converted and high DFF yield (>95%).[11,12] These reports highlight the efficient activity of homogeneous catalysts in this reaction. However, the use of homogeneous catalysts often presents challenges, including equipment corrosion, difficulties in the catalyst reuse, and long work up to purify the product. Various heterogeneous catalysts such as mixed metal oxide ($MgO{\cdot}MnO_2{\cdot}CeO_2$) achieved 98.8% of HMF conversion and 95.2% of DFF yield at 110 °C for 10 h under 20 bar of O_2 pressure, attributed to its basic features that allow the deprotonation of the alcoholic group in the HMF molecule, facilitating the formation of DFF.[13] Nanobelt-arrayed vanadium oxide hierarchical microspheres

[a]Department of Chemistry, University of Liverpool, Crown Street, Liverpool L69 7ZD, UK. E-mail: m.j.rosseinsky@liverpool.ac.uk
[b]Department of Chemistry and Photon Science Institute, The University of Manchester, Manchester, M13 9PL, UK

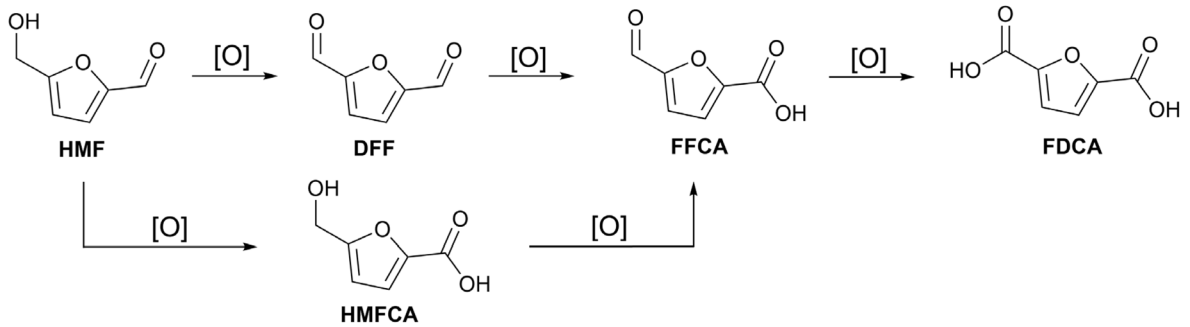

Scheme 1 Possible products from the oxidation of HMF.

led to similar results at 130 °C for 1 h with an O_2 pressure of 30 bar.[14] Ru supported on γ-alumina showed high conversion and yield (both > 90%), but requires harsh conditions (130 °C and 2.7 bar of O_2 pressure).[15] Mesoporous manganese doped cobalt oxide material achieved 80% of HMF conversion and 96% of DFF selectivity in 4 h with DMF as the solvent but a high temperature (130 °C) is necessary.[16] Cu/γ-Al_2O_3 has also been used for the conversion of HMF into DFF at 130 °C by acceptorless dehydrogenation with a DFF yield of 44.9%.[17] The photocatalytic oxidation of HMF to DFF is another promising route to achieving high selectivity. Lead-halide perovskite ($MAPbBr_3$, MA: methylammonium) have been employed, achieving complete HMF conversion with over 90% of DFF yield selectivity after 10 h.[18] Ru complexes supported on CdS quantum dots have also been investigated, with the product distribution influenced by the selective generation of different radical species.[19] More recently, $ZnIn_2S_4$ has been explored as a versatile photocatalyst support, where both incorporation of single Co atoms and cation vacancies have been shown to enhance performance, delivering HMF conversion and DFF yields above 90% up to 12 h.[20,21]

Porous materials have been extensively studied for catalytic applications due to their tuneable porosity and structural diversity, which enable their functionalization as catalyst support and have also been applied in the selective oxidation of HMF to DFF. V_2O_5@Cu-MOR zeolite achieves complete HMF conversion with high DFF yield (91.5%) at 120 °C over a period of 7 h.[22] Covalent triazine frameworks (CTF) also showed high catalytic performance in the selective oxidation of HMF, with high HMF conversion and DFF yield (97.3% and 72.7%, respectively), nevertheless, a reaction temperature of 130 °C is needed.[23] Within the class of porous materials, metal–organic frameworks (MOFs) have significant potential in stabilizing a typically homogeneous catalyst in a heterogeneous form, which is defined as the concept of single-site catalysis.[24–26] MOFs are porous, crystalline, hybrid materials formed by connecting metal cluster with organic linker through metal–carboxyl bond linkages, enabling the construction of extended periodic frameworks.[27,28] Due to their tailored structure and porous characteristics, MOFs are applicable materials for use as catalyst supports.[29] The conversion of HMF to FDCA was demonstrated using polyoxometalates incorporated into Cu-BTC MOF, riboflavin-doped Ni-MOF, and CAU-28.[30–32] Cu species incorporated into UiO-66 were also used to catalyse the conversion of levulinic acid to γ-valerolactone at 140 °C.[33] Additionally, the photocatalytic oxidation of HMF to DFF has been reported utilising MOFs as a catalyst support, with TiO_2@UiO-67-Zr/Ti and noble metal-doped Ti-MOF.[34,35]

In this study, single-site Cu species were incorporated into a MOF-808 framework to develop a heterogenous catalyst designed for use in combination with TEMPO (2,2,6,6-tetramethylpiperidine 1-oxyl) as a co-catalyst. The TEMPO and Cu(II) oxidation mechanism involves the activation of the substrate by Cu(II) and the oxidation by TEMPO•. This synergistic combination is crucial for the selective oxidation of an alcohol into an aldehyde (Scheme 2).[36,37] MOF-808 is a Zr-based MOF with a 6,3-connected three-dimensional framework containing two types of cages with internal pore diameters of 18.4 Å and 4.8 Å, respectively.[38] The MOF-808(Cu) catalysts, with various Cu loadings, were synthesised through post-synthetic modification of MOF-808 and structurally characterised to determine the Cu structure and location. The subsequent catalysts were utilized as a heterogeneous catalyst for the selective catalytic HMF oxidation to DFF to demonstrate the efficacy of single-site metal–organic framework-based catalysts.

2 Results and discussion

2.1 Synthesis and characterisation of MOF-808 and MOF-808(Cu_x)

MOF-808 was synthesised using DMF as the solvent and formic acid as modulator, according to the solvothermal method reported by de Vos *et al.*[39] In the crystal structure of the as-made material each Zr_6 cluster is connected to six benzene tricarboxylate (BTC) linkers and six formate ions that act as capping ligands. After the synthesis, the material undergoes sequential washing with DMF, H_2O, and MeOH over a period of nine days (detailed synthetic procedure described in SI). This process enables the gradual exchange of the DMF contained in the pores with H_2O, and finally with MeOH, in order to fill the pores of the material with a low surface tension molecule that will not damage the structure of the framework during activation (heating under vacuum for 36 h – detailed activation procedure described in SI). Moreover, this process allows the exchange of the capping formate ions with MeO^-/MeOH and $^-OH/H_2O$ on the Zr_6 cluster that will enable its

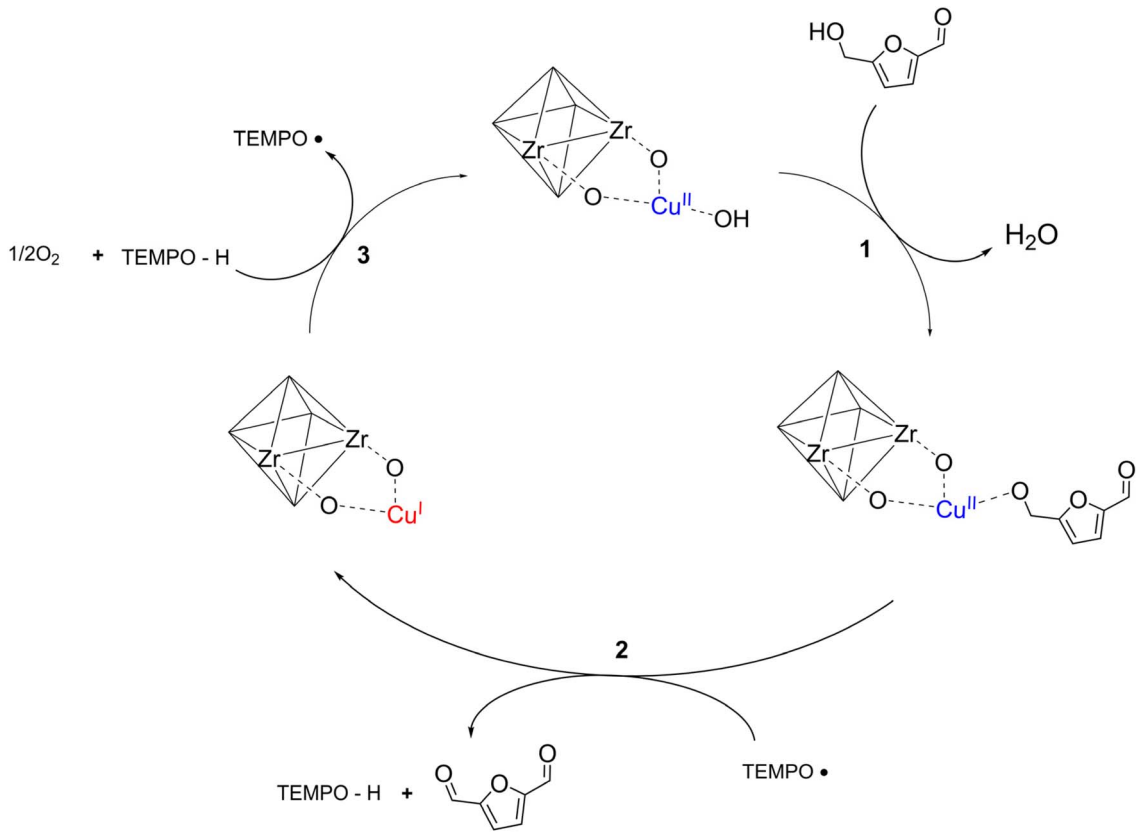

Scheme 2 Proposed reaction mechanism of TEMPO/Cu(II) catalytic oxidation.

functionalisation in the next step.[38–40] This is important as the carboxylate ligands (formate) bind strongly to the Zr_6 cluster and are difficult to remove, whereas, the weakly bound alkoxide ligands (MeO^- and ^-OH) can be easily removed from the Zr_6 cluster, allowing activation of the cluster for the subsequent Cu installation.

Fig. 1a shows the powder X-ray diffraction (PXRD) patterns of the as-made material in DMF (MOF-808 as-made), after the washes (MOF-808 washed), and post-activation (MOF-808 activated). For all materials, the patterns match the simulated pattern of MOF-808. All the observed peaks of the three patterns were indexed in cubic unit cells, with space group $Fd\bar{3}m$ and lattice parameter 35.4476(3) Å for MOF-808 as-made, 35.3855(8) Å for MOF-808 washed and 35.3890(2) Å for MOF-808 activated and confirms that the structure of MOF-808 is retained after the post-synthetic steps.

The chemical composition of MOF-808 was calculated by the combination of thermogravimetric analysis (TGA; Fig. S1) and ^{1}H-NMR using maleic acid as an internal standard (Fig. S2). TGA provides the ratio between inorganic and organic fractions and ^{1}H-NMR shows the relative amount of each organic component. Using this calculation method, the determined chemical formula of activated MOF-808 (Table S2) confirmed that the majority of formate ions, 5.67 out of 6, were exchanged with MeO^-/MeOH and $^-OH/H_2O$.[39]

Activated MOF-808 was then used as a support material to incorporate Cu species by solvothermal reaction with $Cu(NO_3)_2 \cdot 3H_2O$ in DMF at different times and temperatures (procedure given in Section S2.2) to obtain the desired loading (1, 3 and 4 Cu atoms per Zr_6 cluster). The catalysts are denoted MOF-808(Cu_x) where x is the number of Cu atoms per Zr_6 cluster. It is worth noting that in all three procedures, the amount of activated MOF-808 and $Cu(NO_3)_2 \cdot 3H_2O$ used are identical. However, increased reaction times were the key factor in enabling greater Cu incorporation into the MOF structure (Table S1). PXRD patterns of MOF-808(Cu_1), MOF-808(Cu_3), and MOF-808(Cu_4), after synthesis and subsequent activation, are shown in Fig. 1b and demonstrate that the crystallinity of the parent MOF-808 is retained. No other reflections from Cu-containing phases are observed, indicating well-dispersed Cu species. Furthermore, retention of crystal structure is observed after the reaction with $Cu(NO_3)_2 \cdot 3H_2O$ with all the peaks indexed in the cubic unit cell with lattice parameters 35.2692(6) Å, 35.34093(1) Å, and 35.3783(7) Å for MOF-808(Cu_1), MOF-808(Cu_3), and MOF-808(Cu_4) respectively. To confirm the presence of Cu species, energy dispersive X-ray spectroscopy (EDS) measurements were performed on the catalysts, with a homogeneous dispersion of Cu noted in all samples (Fig. S3–S5). The amount of Cu incorporated in the framework was then quantitatively determined using Inductively Coupled Plasma – Optical Emission Spectroscopy (ICP-OES). The determined Cu : Zr_6 cluster ratio in each sample is as follows: 1.23 : 1 for MOF-808(Cu_1), 2.8 : 1 for MOF-808(Cu_3), and 4 : 1 for MOF-808(Cu_4),

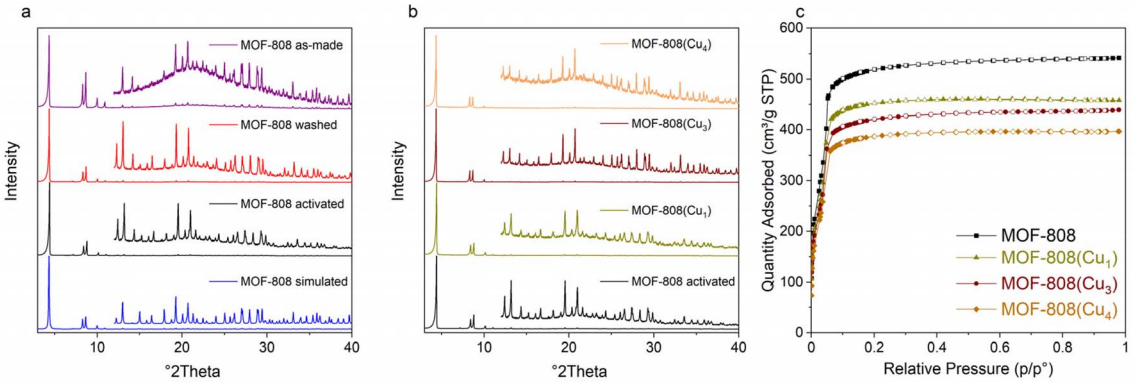

Fig. 1 (a) PXRD of simulated MOF-808 (blue), MOF-808 activated (black), MOF-808 washed (red), and MOF-808 as-made in DMF (purple) [insert: intensity ×30 magnified; insert in MOF-808 as made: intensity ×10 magnified]. (b) PXRD patterns of MOF-808 activated (black), MOF-808(Cu_1) (green), MOF-808(Cu_3) (dark red), and MOF-808(Cu_4) (orange) [insert: intensity ×10 magnified]. (c) N_2 adsorption measurement of MOF-808 (black), MOF-808(Cu_1) (green), MOF-808(Cu_3) (dark red), and MOF-808(Cu_4) (orange). Catalysts are denoted MOF-808(Cu_x) where x is the Cu atoms per Zr_6 cluster.

with full chemical compositions obtained by combination with ^{1}H-NMR (Fig. S6–S8) and given in Table S2.

The N_2 adsorption–desorption isotherms of MOF-808 and MOF-808(Cu_x) samples are reported in Fig. 1c and show the typical type-I(b) isotherm for all the samples, indicating the presence of large micropores. This was additionally confirmed by pore size distribution exhibiting a maximum at 18 Å (Fig. S9). The reduction in BET surface area and total pore volume values of MOF-808(Cu_x) samples compared to MOF-808 (Table 1) is proportional to the increasing loading of Cu and indicates that the Cu species are incorporated within the pores. Scanning electron microscope (SEM) images of MOF-808 activated (Fig. S10) show an octahedral shape of the crystals, with this morphology preserved after Cu incorporation in the three catalysts (Fig. S11–S13). The morphological stability observed by SEM, alongside retention of porosity is in agreement with the PXRD results and confirms stability of the MOF-808 structure upon Cu incorporation.

To determine the speciation and local structure of the loaded Cu species in MOF-808, X-ray absorption spectroscopy (XAS) measurements were conducted on the activated versions of the three catalysts. The Cu X-ray absorption near edge spectroscopy (XANES) spectrum (Fig. 2a) of the samples exhibits notable characteristics. The three samples exhibit a weak pre-edge feature at 8978 eV (insert Fig. 2a), which is associated with the 1s → 3d transition in Cu(II), a dipole transition not allowed for Cu(I) species and thus indicates the presence of Cu(II) in the MOF-808(Cu_x) catalysts.[41]

The *r*-space extended X-ray absorption fine structure spectra (EXAFS) for the three catalysts and the CuO standard are given in Fig. 2b. All spectra show the presence of the Cu–O bond distance (between 1 and 2 Å) but only CuO displays a feature that corresponds to Cu–Cu bond distance (around 3 Å), with the catalysts showing limited extended structures beyond the first shell Cu–O scattering paths. Fitting of the CuO standard and catalysts were undertaken to quantitatively assess the Cu local structure, with fitting parameters and fitting results shown in Table S3. For the fitting of the crystalline CuO standard (fit range $3 \leq k \leq 10$; $1 \leq \Delta R \leq 3.2$), a model of a single scattering Cu–O and Cu–Cu paths with fixed coordination number (CN = 4) was used (Fig. S14), with single scattering paths and CN used in the model determined from the crystal structure of CuO.[42] The fitting of CuO spectra with floating of the disorder parameters ($2\sigma^2$) allowed for calculation of amplitude reduction factor ($S_0{}^2 = 0.852$) that was subsequently used in the fitting of the catalysts. Confirmation of the simple fitting model was given by the wavelet transformation of the CuO standard (Fig. S15a) which shows a strong feature centred at low R (Δk 3–6.5 Å^{-1} and ΔR 1.25–2 Å) associated with the first Cu–O shell with single and multiple scattering paths, and the features ascribed to the first Cu–Cu shell at Δk 5–6 Å^{-1} and ΔR 2–2.5 Å. However, the wavelet transformation of the three catalysts (Fig. S15b–d) shows the absence of the features correlated with the Cu–Cu shell. The MOF-808(Cu_x) samples were then fitted considering a model of single scattering Cu–O path with floating of the CN and $2\sigma^2$ (Table S3 and Fig. S16–S18). The fitting model of the catalysts confirms that the Cu species within MOF-808(Cu_x) do not exhibit Cu–Cu paths, and thus primarily exist as a single site complex in all loadings. The calculated CN values for the Cu–O paths in the three catalysts (3.6(3), 3.5(3), and 3.9(4) for MOF-808(Cu_1), MOF-808(Cu_3), and MOF-808(Cu_4) respectively) confirm that the Cu species are in a square planar geometry, albeit with a slightly lower bond valence than the crystalline

Table 1 BET surface area (S_{BET}) and total pore volume (V_p) values of MOF-808, MOF-808(Cu_1), MOF-808(Cu_3), and MOF-808(Cu_4)

Material	S_{BET} (m^2 g^{-1})	V_p (cm^3 g^{-1})
MOF-808	2190	0.83
MOF-808(Cu_1)	1899	0.71
MOF-808(Cu_3)	1769	0.67
MOF-808(Cu_4)	1605	0.61

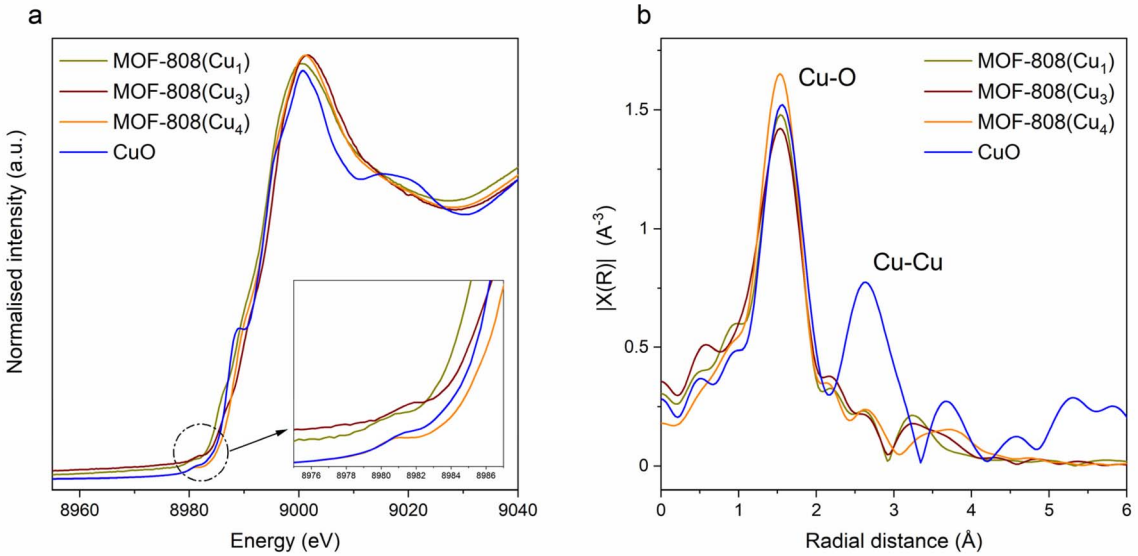

Fig. 2 (a) Experimental XANES spectra for MOF-808(Cu_1) (green), MOF-808(Cu_3) (dark red), MOF-808(Cu_4) (orange), CuO (blue). Insert: expanded pre-edge features from 8978 eV to 8987 Ev. (b) Cu K-edge k^2-weighted EXAFS data in r-space of MOF-808(Cu_1) (green), MOF-808(Cu_3) (dark red), MOF-808(Cu_4) (orange), and CuO (blue).

structure. Furthermore, the path length for the first shell Cu–O is reduced in the catalysts (1.92(1), 1.92(1), and 1.91(1) Å for MOF-808(Cu_1), MOF-808(Cu_3),and MOF-808(Cu_4) respectively) when compared to the experimentally measured crystalline standard CuO (1.95(2) Å) and suggests a different bonding environment to the bulk crystalline structure. The fitting results for the MOF-808(Cu_x) catalysts, with square planar Cu(II) species consisting of Cu–O path lengths (1.91–1.92 Å), are consistent with the results of Garetto *et al.* and the determination of a single site square-planar Cu species, with Cu–O path lengths (1.93 Å), incorporated into UiO-66.[43]

Synchrotron PXRD data of the activated MOF-808(Cu_3) was analysed to construct and refine the structure model, focusing on accurately locating the incorporated Cu within the framework (see Structure refinement process of MOF-808(Cu_3) in SI). Initially the model of MOF-808 crystal structure was refined against the MOF-808(Cu_3) PXRD pattern to locate the Zr_6 cluster and the BTC linker.[38] The Fourier difference map, $F_{obs} - F_{calc}$, revealed regions of high electron density between the terminal O atoms of the neighbouring Zr_6 clusters, which were attributed to the Cu atoms (Fig. S19). A partially occupied Cu site was then located by simulated annealing and is coordinated to the terminal O atom, O3 (Fig. 3). The Cu site is found on the Wyckoff site 96*g* with occupancy value of 0.46, fixed based on the experimentally obtained Cu/Zr ratio. The low occupancy of Cu site combined with the absence of the Cu–Cu bond in EXAFS, suggest that the locally nearest Cu neighbour to each Cu site is vacant, creating isolated Cu sites. The coordination environment of Cu was completed with two O atoms, O4, giving rise to a square planar geometry. A rigid body was used to locate and refine the position of the O4 atom, which could not be identified otherwise, likely due to a combination of low occupancy and complex disorder that is difficult to model. The complex disorder arising from a dynamic coordination shell, also corresponds to the slightly lower than ideal coordination numbers (3.5(3)–3.9(4)) obtained in the EXAFS fitting of the MOF-808(Cu_x) catalysts. The refined model shows Cu–O bond lengths of 1.960(16) Å for Cu–O3 and 1.92 Å for Cu–O4, which is comparable with the averaged Cu–O path lengths obtained from EXAFS measurements (~1.92 Å; Table S3). The Rietveld fit and crystallographic information are provided in Fig. S20 and Table S4.

In summary, Cu single site species supported within MOF-808 porous frameworks were successfully synthesised. Retention of the porous structure of the framework after installation of Cu was confirmed by a combination of PXRD, SEM, and adsorption measurements. Various loadings of Cu atoms could also be achieved through alteration of the Cu installation reaction conditions. The location and geometry of the Cu sites were determined through a combination of synchrotron methods, utilising XAS and PXRD refinements, with the square planar Cu(II) sites shown to exist in partially occupied positions attached to the Zr_6 cluster through bridging oxygens. Importantly, this combination of advanced modelling techniques allowed for the construction of a structure model of the Cu species within the framework.

2.2 HMF catalytic oxidation

The synthesised MOF-808(Cu_x) catalysts were evaluated in the selective catalytic oxidation of HMF to DFF at 30 °C at various time points in acetonitrile, with TEMPO and fixed Cu mmol loading. Reactions and analysis by HPLC were conducted in triplicate, with standard deviation reported as errors of multiple reactions. Fig. 4 shows the catalytic performances of MOF-808(Cu_1), MOF-808(Cu_3), and MOF-808(Cu_4). HMF conversion was 94.4 ± 4.4% with MOF-808(Cu_1), 95.5 ± 2.7% with MOF-808(Cu_3), and 81.5 ± 0.7% with MOF-808(Cu_4). While the

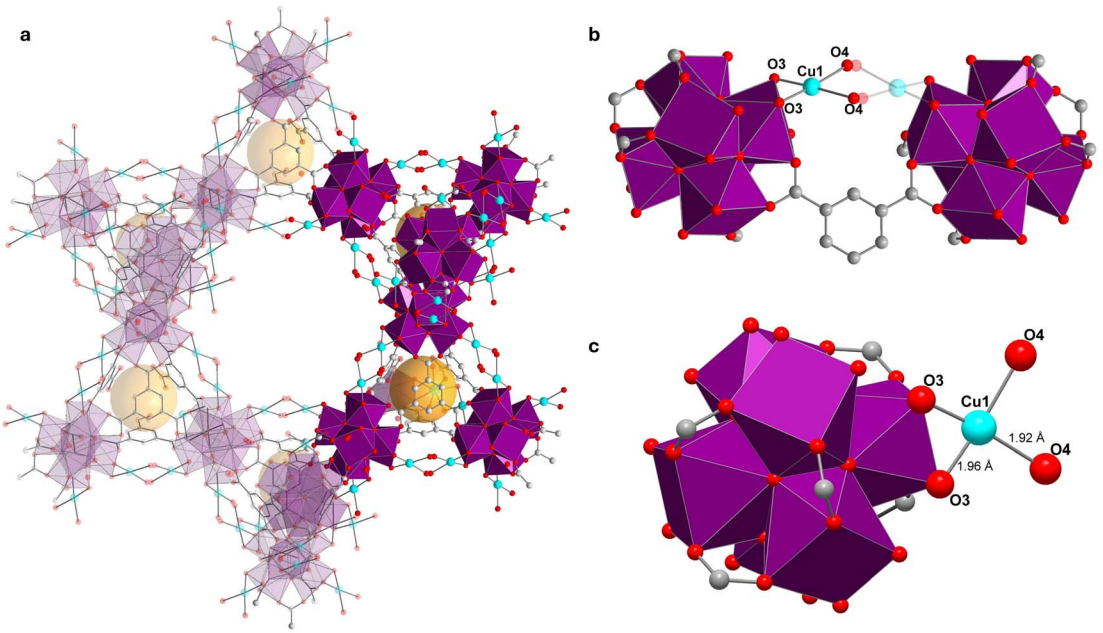

Fig. 3 (a) Structural depiction of the incorporated Cu in the MOF-808(Cu_3) structure, showing all possible crystallographically identical Cu sites within the MOF-808 crystal structure in relation to the adamantane and tetrahedral cages. (b) Two Zr_6 clusters connected by the BTC linker are shown alongside the incorporated Cu. However, the low occupancy of Cu and the absence of Cu–Cu paths in the EXAFS fitting, indicates that the nearest Cu neighbour to each Cu site is vacant, creating isolated Cu sites. (c) One Zr_6 cluster is shown with the Cu coordination environment with the Cu–O lengths labelled as obtained through a combination of PXRD refinement and EXAFS analysis. The $[Zr_6O_4(OH)_4]^{12+}$ clusters are shown with purple polyhedra of Zr atoms coordinated by O atoms in red. The BTC linker carbon atoms are shown in grey, and the Cu atoms in light blue. The yellow spheres in (a) represent the guest-accessible tetrahedral cages. H atoms are omitted for clarity from all depictions.

conversion rates were comparable, the differences in DFF yields were more pronounced, with MOF-808(Cu_1) achieving a DFF yield of 53.3 ± 7.1%, 78.9 ± 1.3% with MOF-808(Cu_3), and 67.9 ± 1.5% with MOF-808(Cu_4). It is worth noting that MOF-808(Cu_3) exhibits activity at milder reaction conditions than reported heterogeneous catalysts used for this reaction, with comparable DFF yields (Table S5).[13,14,23]

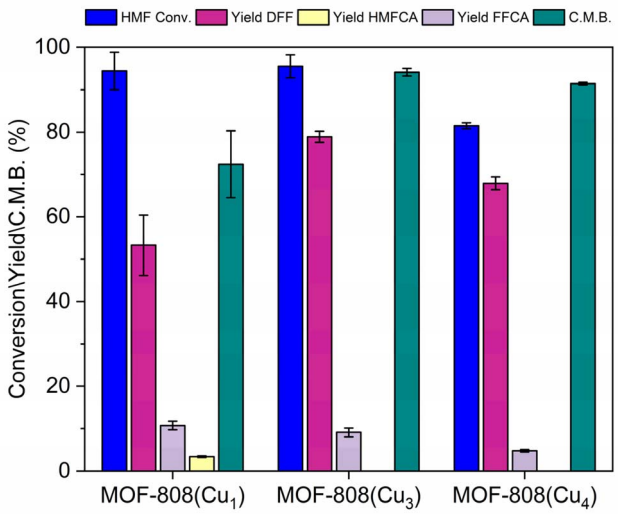

Fig. 4 Results of the catalytic HMF oxidation over MOF-808(Cu_x), where x = Cu atom per Zr_6 cluster. Reaction conditions: HMF (0.1 mmol, 12.6 mg), TEMPO (0.1 mmol, 15.6 mg), catalyst (30 mmol % of Cu), acetonitrile (4 mL), 600 rpm, 30 °C, 12 h. (HMF: 5-hydroxymethylfurfural; DFF: 2,5-diformylfuran; HMFCA: 5-fydroxymethyl-2-furancarboxylic acid; FFCA: 5-formyl-2-furancarboxylic acid; CMB: carbon mass balance).

The reaction pathway of HMF oxidation (Scheme 1) was validated through the formation of additional products during the reaction. With MOF-808(Cu_1), a small amount of HMFCA (3.4 ± 0.2%) was detected, indicating the oxidation of the aldehyde group of HMF. Interestingly, HMFCA was not observed when MOF-808(Cu_3) or MOF-808(Cu_4) were used as catalysts, but a small amount of FFCA was produced (9.1 ± 1% and 4.8 ± 0.3% respectively). Notably, no FDCA was produced in any of the reactions, indicating that the catalyst system does not facilitate the overoxidation of HMF to form the dicarboxylic acid derivative under the reaction conditions utilised. Differences in the carbon mass balance (CMB) become also apparent, with CMB values for the reactions for MOF-808(Cu_3) and MOF-808(Cu_4) almost identical (94.1 ± 0.9% and 91.4 ± 0.3% respectively). In contrast, the CMB dropped significantly to 72.4 ± 7.9% for MOF-808(Cu_1). CMB values below 100% corresponds to the formation of products that cannot be detected by HPLC, which are likely to be humins, oligomeric byproducts that arise from the condensation of reaction intermediates.[44,45] The differences in catalytic selectivity between the MOF-808(Cu_x), despite mass fixed Cu loading with comparable local structures, suggests an influence related to Cu density and possible co-operative transformations between closely located Cu sites, as reported for high loading geminal-atom Cu catalysts for cross

coupling reactions.[46] However, it worth noting that MOF-808(Cu_1) is the only one that shows HMFCA formation after 12 h. Nevertheless, it needs to be pointed out that during the time course study of MOF-808(Cu_3) HMFCA is formed after 4 h of reaction (2%) and it disappears after 6 h (Fig. S21). These results suggest that even MOF-808(Cu_3) produces HMFCA during the reaction but, due to the higher catalytic activity, it is converted to other products by the end of the 12 h of reaction.

The catalytic oxidation of HMF using MOF-808(Cu_x) was further investigated at various temperatures ranging from 30 °C to 80 °C (Fig. S22a). HMF conversion was complete under all conditions, however DFF yield decreased with higher temperatures due to the reactivity of DFF under harsher conditions. Fixing the reaction temperature at 30 °C, the effect of TEMPO concentration (0.01, 0.05, 0.1 mmol) was assessed (Fig. S22b). HMF conversion and DFF yield increased with higher concentration of TEMPO, with the highest conversion at 95.5% and DFF yield of 78.9% with 0.1 mmol of TEMPO. The strong effect of TEMPO concentration highlights the crucial nature of TEMPO in the oxidation cycle.

To further evaluate the role of the individual components of the catalyst system, catalytic control reactions were undertaken (Fig. 5a). Initially, a homogeneous $Cu(NO_3)_2 \cdot 3H_2O$ was tested with TEMPO, under the same reaction conditions and shows significant catalytic activity with a conversion of HMF of 98.8 ± 1.4% and a DFF yield of 93.1 ± 9.4% in agreement with literature results.[12] Although $Cu(NO_3)_2$ exhibits high catalytic activity in the selective oxidation of HMF to DFF, in-combination with TEMPO, the homogeneous nature of $Cu(NO_3)_2$ limits industrial applicability when compared to the heterogeneous MOF-808(Cu_x) catalysts. This is mainly due to associated technical challenges, such as equipment corrosion, difficulties in catalyst recovery, and extensive purification steps. Then, the activity of the co-catalyst TEMPO was examined independently, without the presence of Cu-catalyst in the reaction mixture. TEMPO was found to convert 13 ± 5.2% of HMF, yielding almost no DFF (0.2% yield). Activated MOF-808 without Cu with TEMPO under the standard reaction conditions resulted in 24.6 ± 7.8% of HMF conversion and 4.7 ± 0.7% of DFF yield. Finally, the activity of MOF-808(Cu_3) was tested without TEMPO, and results in a HMF conversion of 10.9 ± 1% and no yield of DFF. Therefore, the catalytic and control reaction results confirm the crucial combination of Cu and TEMPO required for the catalytic activity and selectivity.

MOF-808(Cu_3) was utilized for a time course study, during which reactions were tested at different time intervals of as illustrated in Fig. 5b. After 1 h, the HMF conversion reached 34.2 ± 4.8% with a corresponding DFF yield of 19.2 ± 3.8%. Complete conversion, within error, was achieved at 12 h, with the highest DFF yield of 78.9 ± 1.3%. A hot filtration test was then conducted to determine the nature of the selective catalytic oxidation reaction. The catalyst was removed *via* filtration after 1 h, with the reaction continued for another 11 h. Analysis of the reaction mixture after the catalyst filtration and a further 11 h (Fig. 5b) shows 36.7 ± 4% of HMF conversion, confirming that no further HMF is converted once the catalyst is removed and thus supporting its heterogeneous nature. A decrease in DFF yield is also observed after the catalyst removal, dropping from 19.2 ± 3.8% at 1 h to 11.2 ± 0.6% at 12 h. This decrease is attributed to the reactive nature of DFF, which contains two aldehydic groups in its structure, making it susceptible to gradual conversion into oligomeric species and loss of carbon mass balance over time. This result highlights the necessity of the heterogeneously defined square planar Cu species, which stabilise the transition states of the reactant and intermediates during the catalytic cycle and thereby increasing the rates of selective oxidation to DFF, beyond that of the competitive radical polymerisation side reactions.

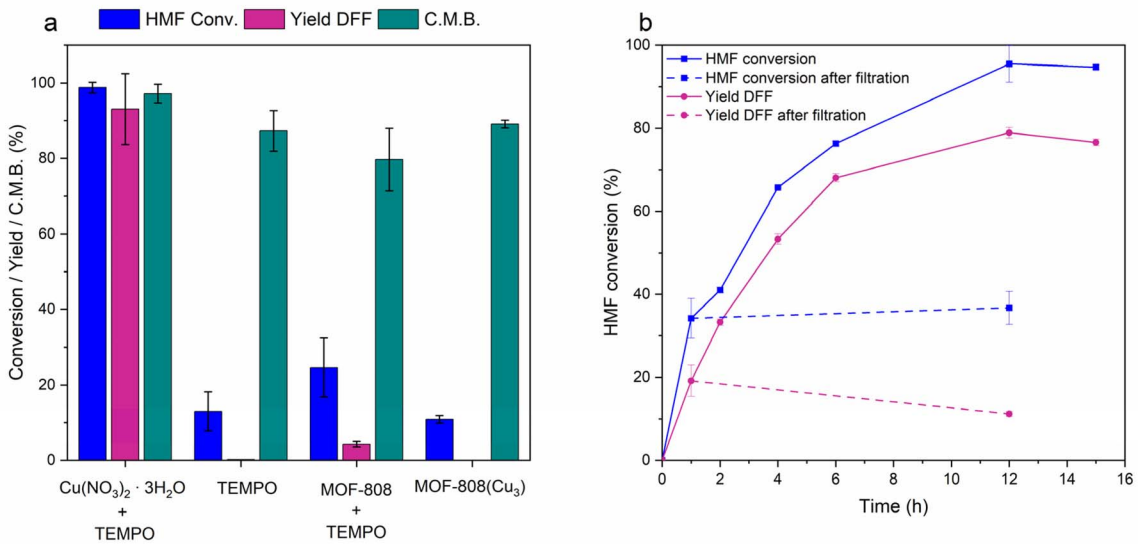

Fig. 5 (a) Catalytic control tests using $Cu(NO_3)_2 \cdot 3H_2O$, TEMPO, activated MOF-808, and MOF-808(Cu_3) as catalyst. (b) Time course study and Hot filtration test. Reactions conditions: HMF (0.1 mmol, 12.6 mg); TEMPO (0.1 mmol, 15.6 mg); MOF-808(Cu_3) (30 mmol % of Cu); acetonitrile (4 mL); 600 rpm; 30 °C; time. (HMF: 5-hydroxymethylfurfural; DFF: 2,5-diformylfuran; CMB: carbon mass balance).

This is demonstrated with the proposed mechanism (Scheme 2), based on previous literature which established the roles of Cu(II) and TEMPO in facilitating selective oxidative transformations.[36,37] In this system, Cu(II) plays an important role by deprotonating and coordinating to the oxygen atom of the alcohol, with a corresponding release of H_2O (Scheme 2, step 1). The activated intermediate species has increased reactivity on the alcoholic carbon, allowing the removal of hydrogen on the alcoholic carbon by TEMPO$^{\bullet}$ and Cu(II). The TEMPO$^{\bullet}$ species are reduced to TEMPOH, and Cu(II) is reduced to Cu(I) (Scheme 2, step 2) in single electron pathways (homolytic cleavage) and yields the oxidised DFF. The final step is the regeneration of TEMPO$^{\bullet}$ through activation of O_2 over the Cu species (Scheme 2, step 3). Competitive side reactions yielding HMFCA or the further oxidised product FFCA occur through binding of the aldehyde position of HMF or DFF and the subsequent oxidation cycle produces the carboxylic acid moiety.[47,48] Furthermore, the minor loss of carbon mass balance in the reactions suggests formation of oligomeric species that are obtained through competitive uncontrolled radical pathways during cleavage, as reported in literature.[44,45]

To investigate the catalytic conversion of HMF to DFF and the involvement of radical intermediates, electron paramagnetic resonance (EPR) studies were conducted on a reaction mixture of MOF-808(Cu_3), HMF, and TEMPO in acetonitrile. Control experiments with single components and solvent (Fig. S24a) showed no signal for HMF, while the catalyst in solid state or dispersed in acetonitrile exhibited a very weak Cu(II) signal (~3200 G). The reaction mixture was then analysed *in situ* at different time points to monitor the formation of any radical species. The spectra displayed a consistent characteristic three-line pattern of TEMPO due to the interaction of an electron spin with the ^{14}N nucleus (Fig. S24b). It is important to note that the strong signal of TEMPO masked Cu(II) species or any weak or transient signals from reaction intermediates, preventing clear observation of new radical species.

To further investigate the possible formation of short-lived radicals under the heterogeneous catalytic conditions, radical trapping experiments using 5,5-dimethyl-1-pyrroline *N*-oxide (DMPO) were performed (Fig. S25). Control experiments performed show no signals were observed when DMPO was added to acetonitrile alone or with HMF, while in the presence of

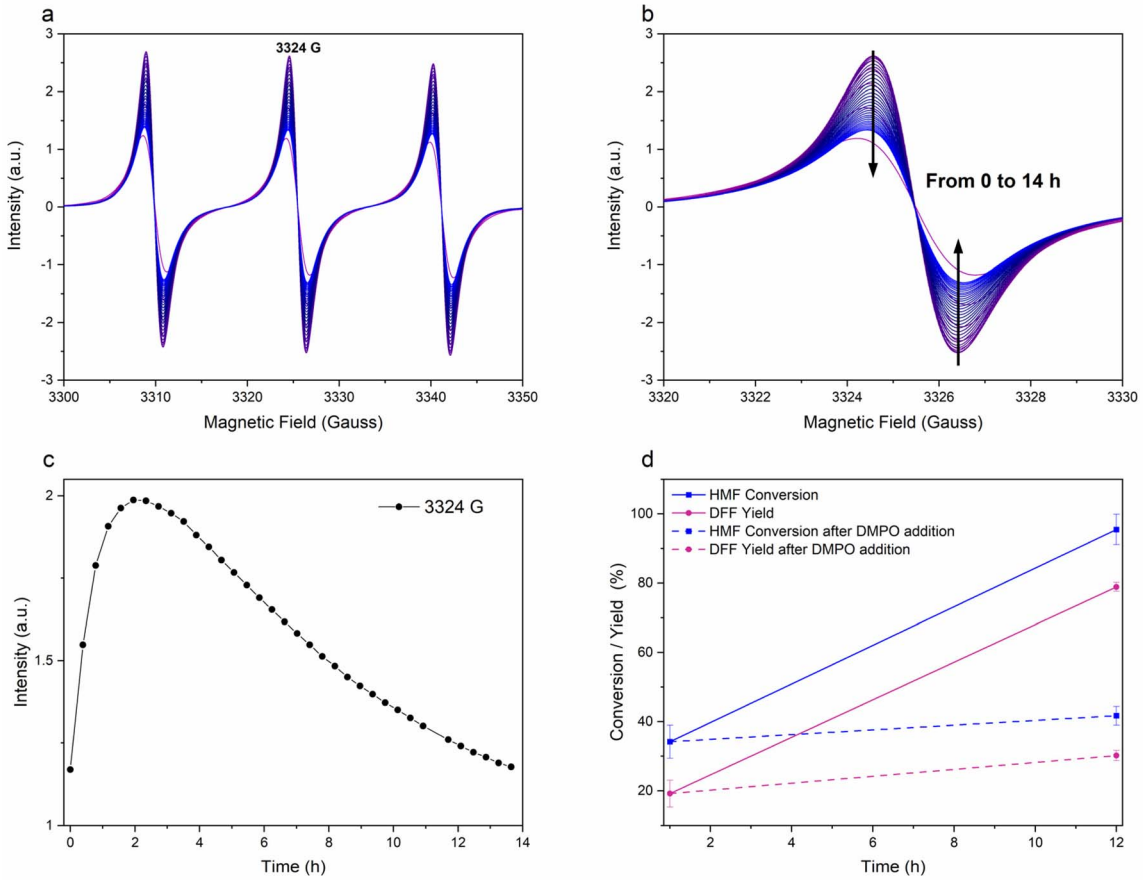

Fig. 6 (a) *In situ*, time dependent cw-EPR spectra of MOF-808(Cu_3) (30% mmol of Cu), HMF (0.1 mmol, 12.6 mg), TEMPO (0.1 mmol, 15.6 mg) dissolved in acetonitrile (4 mL) in the presence of DMPO (0.88 mmol, 100 mg) over a time period of 14 h. (b) Expanded TEMPO EPR signal from 3320 G to 3330 G. The black arrow indicates the direction of the variation in the signal amplitude over the time. (c) Amplitude of the TEMPO EPR signal at 3324 G plotted as a function of time (h). (d) Results of the HMF catalytic oxidation in the presence of DMPO added after 1 h of reaction. Reaction conditions: MOF-808(Cu_3) (30% mmol of Cu), HMF (0.1 mmol, 12.6 mg), TEMPO (0.1 mmol, 15.6 mg) dissolved in acetonitrile (4 mL) in the presence of DMPO (0.88 mmol, 100 mg). (HMF: 5-hydroxymethylfurfural; DFF: 2,5-diformylfuran).

TEMPO the spectrum was dominated by the TEMPO signal. When DMPO was mixed with MOF-808(Cu_3) in acetonitrile, a distinct nitroxide signal was observed. The observed hyperfine coupling to the nitroxyl ^{14}N (nuclear spin $I = 1$; $a_{iso}(^{14}N) = 13.1$ G) and β-^{1}H ($I = 1/2$; $a_{iso}(^{1}H) = 7.98$ G) nuclei implies the formation of a DMPO-oxygen adduct, providing evidence of the formation of oxygen radicals during the catalytic conversion of HMF to DFF.[49,50] The presence of activated oxygen species corresponds to the proposed mechanism by Stahl and co-workers.[36,37,51]

The involvement of oxygen radical species in the proposed catalytic mechanism (Scheme 2, step 3) was further validated by monitoring the heterogeneous reaction *in situ* over 14 h in the presence of DMPO. No new EPR signals were observed during the reaction (Fig. 6a) due to the predominance of the TEMPO signal, but a decrease in the amplitude of TEMPO signal over time is noted (Fig. 6b). The amplitude of the TEMPO signal at 3324 G plotted as a function of time (Fig. 6c), clearly shows the consumption of the TEMPO radical. This occurs as DMPO traps the activated oxygen radicals that are generated over Cu species, forming a DMPO-oxygen adduct, and thus interrupting the catalytic cycle by stopping the regeneration of TEMPO radical from TEMPO-H. To directly assess the impact of DMPO on the catalytic system, the oxidation of HMF to DFF was performed with addition of DMPO. The reaction was first carried out under standard conditions for 1 h, after which 100 mg of DMPO (0.88 mmol) was added and the mixture was allowed to proceed for a further 11 h. The addition of DMPO inhibited HMF conversion and DFF formation (Fig. 6d). This outcome is consistent with the EPR data and confirms that activated oxygen species and TEMPO radicals participate in the catalytic process, playing a crucial role in the redox cycle of TEMPO/TEMPO-H and Cu(I)/Cu(II) (Scheme 2, step 3).

2.3 Recyclability test and catalyst deactivation study

The recyclability of MOF-808(Cu_3) was tested in multiple cycles of the HMF catalytic oxidation (Fig. 7). Post each reaction cycle, the catalyst was collected by centrifugation and dried under vacuum at 60 °C for 3 h and then used for the next cycle. The catalyst mass was kept consistent across multiple cycles through multiple repetitions of each cycle. The catalyst shows a gradual decline in the catalytic activity each cycle, with HMF conversion decreasing from 95.5 ± 2.7% in the first cycle to 87 ± 2.6% in the second and 73.7 ± 6.4% in the third. Notably, while HMF conversion decreases by approximately 10% per cycle, the DFF yield does not follow the same trend. Instead, after the first cycle it drops from 78.9 ± 1.3% to 70.6 ± 4% and then reaches 44.3 ± 1.5% after the third cycle.

Structure and compositional characterisation of the used catalyst after one cycle was performed in order to investigate the reduction in catalytic activity. ICP-OES results show that after one reaction cycle, the Cu content in the MOF decreased by 20%. Additionally, EXAFS results of the spent catalyst reveal the formation of particles, indicated by the presence of the Cu–Cu bond distance (Fig. S26), which could be responsible for the reduced selectivity. However, despite partial Cu leaching, post-reaction characterisations confirm the structure stability by the retention of crystallinity and shape of the MOF crystals (Fig. S27–S29).

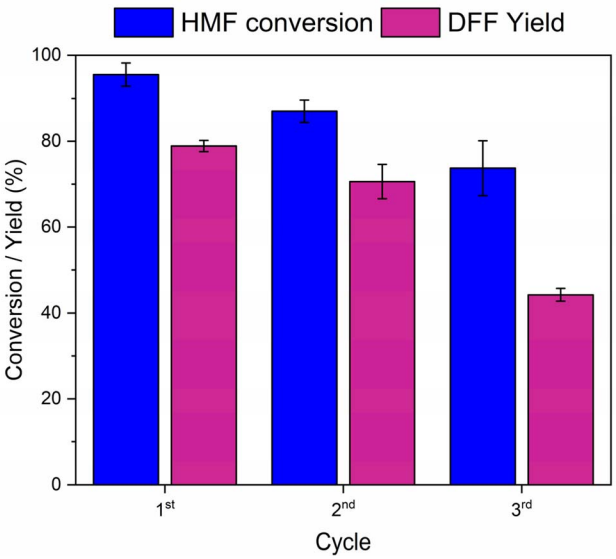

Fig. 7 Recycling experiment of MOF-808(Cu_3). Reaction conditions: HMF (0.1 mmol, 12.6 mg); TEMPO (0.1 mmol, 15.6 mg); MOF-808(Cu_3) (30 mmol % of Cu); acetonitrile (4 mL); 600 rpm; 30 °C; 12 h. (HMF: 5-hydroxymethylfurfural; DFF: 2,5-diformylfuran).

To determine the significant factor in Cu leaching, the stability of the catalyst in the individual reaction components (solvent, TEMPO, HMF, or DFF) was examined by conducting separate tests for 12 h, followed by ICP-OES analysis of the Cu content in the spent catalyst, as well as the Cu leached in the reaction media (Table S6). In the first test, the catalyst and solvent (acetonitrile) were tested under standard conditions, with Cu atoms per Zr_6 cluster (2.86) similar to the fresh catalyst (2.96), confirming that there is limited influence of the solvent on the catalyst. For the individual test with HMF or DFF in acetonitrile, a slight reduction in Cu atoms per Zr_6 cluster was observed (2.83 and 2.68, respectively), indicating a minor effect of the coordinating organic components. However, TEMPO was identified as the primary cause of Cu leaching, with the number of Cu atoms per Zr_6 cluster reduced to 1.46 in the spent catalyst, from 2.96 in the fresh catalyst. These results show that the coordination and cycling of the co-catalyst TEMPO to Cu atoms during the catalytic cycle, leads to their abstraction from the Zr_6 cluster *via* solubilization in the reaction mixture. Nevertheless, the catalyst system demonstrates that high catalytic activity and selectivity under near ambient reaction conditions can be achieved using defined single Cu-site catalysts that utilise porous metal–organic frameworks. However, further work is required to stabilise the Cu sites under liquid phase conditions in tandem with less aggressive co-catalysts.

3 Conclusions

Anchoring of Cu(II) on MOF-808 was achieved by solvothermal reaction that delivered highly ordered and porous catalysts with

varying content of Cu. The structure model of MOF-808(Cu_3) was obtained by XAS and Rietveld refinement of PXRD pattern, illustrating the single Cu(II) species in a square planar geometry attached to the Zr_6 cluster through bridging O of the capping ligands. The catalysts were tested for the selective oxidation of HMF to DFF, with MOF-808(Cu_3) exhibiting the highest DFF yield under near ambient conditions. The crucial role of the solid catalyst in the reaction was demonstrated through hot filtration experiments, where the yield of DFF dropped after removal of MOF-808(Cu_3), and no catalytic conversion of HMF was noted. The catalyst retains its crystallinity and morphology after the catalytic test, which underscores the stability of the framework support. This work highlights the potential of utilising metal organic frameworks as supports for single site Cu species and their application as oxidation catalysts.

Author contributions

Fabio Raspante: conceptualization, methodology, validation, investigation, writing – original draft. Xiang Zhou: conceptualization, methodology, validation, investigation. Donald R. Inns: methodology, validation, investigation, writing – review & editing. Nusik Gedikoglu Lauritzen: formal analysis. Muralidharan Shanmugam: methodology, formal analysis. Adam Brookfield: methodology, formal analysis. Alexandros P. Katsoulidis: conceptualization, methodology, writing – review & editing, supervision. Matthew J. Rosseinsky: conceptualization, writing – review & editing, supervision, funding acquisition.

Conflicts of interest

The authors declare that they have no known competing financial interests or personal relationships that could influence the work reported in this paper.

Data availability

Metadata (PXRD, TGA, N_2 adsorption measurement, and XAS) for this article is also available *via* the University of Liverpool data repository at **https://doi.org/10.17638/datacat.liverpool.ac.uk/3018**.

CCDC 2464790 contains the supplementary crystallographic data for this paper.[52]

The data supporting this article have been included as part of the supporting information (SI). Supplementary information: additional experimental data and supporting figures. See DOI: **https://doi.org/10.1039/d5ta04979b**.

Acknowledgements

The authors acknowledge funding from EPSRC and Unilever through the Cleaner Futures Prosperity Partnership (EP/V038117/1). The authors would like to acknowledge the support of the Materials Innovation Factory at the University of Liverpool, created as part of the UK Research Partnership Investment Fund (UKRPIF) initiative, managed by UKRI Research England. XAS measurements were performed at Diamond Light Source on beamline B18 through the UK Catalysis Hub BAG (Proposal SP34632-1, SP34632-5). The authors also thank Diamond Light Source for access to beamline I11 for the diffraction measurements (Proposal CY31578-7 and CY31578-8). MS and AdB acknowledge the financial support from The University of Manchester and the EPSRC. All authors thank the EPSRC for funding of the EPR National Facility at Manchester (EP/W014521/1).

References

1 D. Wang, H. Shan, W. Yin and H. Li, *Fuel*, 2024, **355**, 129439.
2 J.-Y. Chen, Y. Xiao, F.-S. Guo, K.-M. Li, Y.-B. Huang and Q. Lu, *ACS Catal.*, 2024, **14**, 5198–5226.
3 K. Gupta, R. K. Rai and S. K. Singh, *ChemCatChem*, 2018, **10**, 2326–2349.
4 W.-W. Zhao, C.-Y. Zhang, Z.-G. Yan, L.-P. Bai, X. Wang, H. Huang, Y.-Y. Zhou, Y. Xie, F.-S. Li and J.-R. Li, *J. Chromatogr. A*, 2014, **1370**, 121–128.
5 A. A. Turkin, E. V. Makshina and B. F. Sels, *ChemSusChem*, 2022, **15**, e202200412.
6 N. Perret, A. Grigoropoulos, M. Zanella, T. D. Manning, J. B. Claridge and M. J. Rosseinsky, *ChemSusChem*, 2016, **9**, 521–531.
7 C. Chen, M. Lv, H. Hu, L. Huai, B. Zhu, S. Fan, Q. Wang and J. Zhang, *Adv. Mater.*, 2024, **36**, 2311464.
8 R. Ramos, A. Grigoropoulos, B. L. Griffiths, A. P. Katsoulidis, M. Zanella, T. D. Manning, F. Blanc, J. B. Claridge and M. J. Rosseinsky, *J. Catal.*, 2019, **375**, 224–233.
9 M. Del Poeta, W. A. Schell, C. C. Dykstra, S. K. Jones, R. R. Tidwell, A. Kumar, D. W. Boykin and J. R. Perfect, *Antimicrob. Agents Chemother.*, 1998, **42**, 2503–2510.
10 A. Gandini and N. M. Belgacem, *Polym. Int.*, 1998, **47**, 267–276.
11 T. S. Hansen, I. Sádaba, E. J. García-Suárez and A. Riisager, *Appl. Catal., A*, 2013, **456**, 44–50.
12 M. Hong, J. Min, S. Wu, H. Cui, Y. Zhao, J. Li and S. Wang, *ACS Omega*, 2019, **4**, 7054–7060.
13 F. Nocito, M. Ventura, M. Aresta and A. Dibenedetto, *ACS Omega*, 2018, **3**, 18724–18729.
14 Y. Yan, K. Li, J. Zhao, W. Cai, Y. Yang and J.-M. Lee, *Appl. Catal., B*, 2017, **207**, 358–365.
15 C. A. Antonyraj, J. Jeong, B. Kim, S. Shin, S. Kim, K.-Y. Lee and J. K. Cho, *J. Ind. Eng. Chem.*, 2013, **19**, 1056–1059.
16 S. Biswas, B. Dutta, A. Mannodi-Kanakkithodi, R. Clarke, W. Song, R. Ramprasad and S. L. Suib, *Chem. Commun.*, 2017, **53**, 11751–11754.
17 X. Gao, Z. Li, S. Zhang, D. Zhang, X. Zhao, B. Zhang and Y. Wang, *Chem. Eng. J.*, 2024, **496**, 153775.
18 M. Zhang, Z. Li, X. Xin, J. Zhang, Y. Feng and H. Lv, *ACS Catal.*, 2020, **10**, 14793–14800.
19 T. Xia, W. Gong, Y. Chen, M. Duan, J. Ma, X. Cui, Y. Dai, C. Gao and Y. Xiong, *Angew Chem. Int. Ed. Engl.*, 2022, **61**, e202204225.
20 X. Tan, S. Si, D. Xiao, X. Bao, K. Song, Z. Wang, Y. Liu, Z. Zheng, P. Wang, Y. Dai, B. Huang and H. Cheng, *ACS Catal.*, 2023, **13**, 14395–14403.

21 J. Zhao, Y. Wang, H. Liu, R. Zhang, W. Jia, J. Zhang, Y. Sun and L. Peng, *ACS Catal.*, 2025, **15**, 3464–3474.
22 W. Zhang, J. Xie, W. Hou, Y. Liu, Y. Zhou and J. Wang, *ACS Appl. Mater. Interfaces*, 2016, **8**, 23122–23132.
23 J. Artz, S. Mallmann and R. Palkovits, *ChemSusChem*, 2015, **8**, 672–679.
24 J. M. Thomas, R. Raja and D. W. Lewis, *Angew. Chem., Int. Ed.*, 2005, **44**, 6456–6482.
25 A. Grigoropoulos, G. F. S. Whitehead, N. Perret, A. P. Katsoulidis, F. M. Chadwick, R. P. Davies, A. Haynes, L. Brammer, A. S. Weller, J. Xiao and M. J. Rosseinsky, *Chem. Sci.*, 2016, **7**, 2037–2050.
26 A. Grigoropoulos, A. I. McKay, A. P. Katsoulidis, R. P. Davies, A. Haynes, L. Brammer, J. Xiao, A. S. Weller and M. J. Rosseinsky, *Angew. Chem., Int. Ed.*, 2018, **57**, 4532–4537.
27 O. M. Yaghi, *J. Am. Chem. Soc.*, 2016, **138**, 15507–15509.
28 Z. Hu, I. Castano, S. Wang, Y. Wang, Y. Peng, Y. Qian, C. Chi, X. Wang and D. Zhao, *Cryst. Growth Des.*, 2016, **16**, 2295–2301.
29 V. R. Remya and M. Kurian, *Int. Nano Lett.*, 2018, **9**, 17–29.
30 P. Koley, S. C. Shit, T. Yoshida, H. Ariga-Miwa, T. Uruga, T. Hosseinnejad, S. Periasamy, S.-I. In, D. D. Mandaliya, R. D. Gudi, Y. Iwasawa and S. K. Bhargava, *ACS Catal.*, 2023, **13**, 6076–6092.
31 P. Sekar, P. Vasanthakumar, R. Shanmugam, S. Senthil Kumar, S. Agnoli, R. J. Deepak, K. Murugan, N. Bhuvanesh and R. Karvembu, *Green Chem.*, 2022, **24**, 9233–9244.
32 S. as, G. Cibin and R. I. Walton, *ACS Sustain. Chem. Eng.*, 2024, **12**, 5575–5585.
33 Y. Wu, H. Wang, J. Peng, J. Zhang and M. Ding, *Chem. Eng. J.*, 2023, **454**, 140156.
34 Y. Zhou, J. Liu and J. Long, *J. Solid State Chem.*, 2021, **303**, 122510.
35 P. Qiu, Y. Yao, S. Lu, L. Chen, Y. Chen and X. Liao, *Fuel*, 2023, **351**, 129043.
36 B. L. Ryland and S. S. Stahl, *Angew. Chem., Int. Ed.*, 2014, **53**, 8824–8838.
37 J. M. Hoover, B. L. Ryland and S. S. Stahl, *J. Am. Chem. Soc.*, 2013, **135**, 2357–2367.
38 H. Furukawa, F. Gandara, Y. B. Zhang, J. Jiang, W. L. Queen, M. R. Hudson and O. M. Yaghi, *J. Am. Chem. Soc.*, 2014, **136**, 4369–4381.
39 C. Jia, F. G. Cirujano, B. Bueken, B. Claes, D. Jonckheere, K. M. Van Geem and D. De Vos, *ChemSusChem*, 2019, **12**, 1256–1266.
40 N. Marquardt, M. Dahlke and A. Schaate, *ChemPlusChem*, 2023, **88**, e202300109.
41 S. Guan, P. R. Davies, E. K. Gibson, D. Lennon, G. E. Rossi, J. M. Winfield, J. Callison, P. P. Wells and D. J. Willock, *Faraday Discuss.*, 2018, **208**, 67–85.
42 O. García-Martínez, R. M. Rojas, E. Vila and J. L. M. de Vidales, *Solid State Ionics*, 1993, **63–65**, 442–449.
43 B. Garetto, N. Cao, V. Finelli, E. Aunan, M. Signorile, U. Olsbye, S. Bordiga, A. Nova and E. Borfecchia, *J. Phys. Chem. C*, 2025, **129**, 3570–3582.
44 J. C. Velasco Calderon, J. S. Arora and S. H. Mushrif, *ACS Omega*, 2022, **7**, 44786–44795.
45 E. de Jong, M. Mascal, S. Constant, T. Claessen, P. Tosi and A. Mija, *Green Chem.*, 2025, **27**, 3136–3166.
46 X. Hai, Y. Zheng, Q. Yu, N. Guo, S. Xi, X. Zhao, S. Mitchell, X. Luo, V. Tulus, M. Wang, X. Sheng, L. Ren, X. Long, J. Li, P. He, H. Lin, Y. Cui, X. Peng, J. Shi, J. Wu, C. Zhang, R. Zou, G. Guillen-Gosalbez, J. Perez-Ramirez, M. J. Koh, Y. Zhu, J. Li and J. Lu, *Nature*, 2023, **622**, 754–760.
47 D. Leifert and A. Studer, *Chem. Rev.*, 2023, **123**, 10302–10380.
48 M. Zhao, J. Li, E. Mano, Z. Song, D. M. Tschaen, E. J. J. Grabowski and P. J. Reider, *J. Org. Chem.*, 1999, **64**, 2564–2566.
49 Y. L. S. Kim, K. M. Nash, J. L. Zweier, A. Rockenbauer and F. A. Villamena, *JACS Au*, 2010, **132**, 17157–17173.
50 F. A. Villamena, *J. Phys. Chem. A*, 2010, 1153–1160.
51 J. Rabeah, U. Bentrup, R. Stosser and A. Bruckner, *Angew Chem. Int. Ed. Engl.*, 2015, **54**, 11791–11794.
52 CCDC 2464790: Experimental Crystal Structure Determination, 2025, DOI: **10.5517/ccdc.csd.cc2nqtcl**.